JFM RAPIDS
journals.cambridge.org/rapids

Inverse Magnus effect on a rotating sphere: when and why

Jooha Kim[1], Haecheon Choi[1,2,†], Hyungmin Park[1] and Jung Yul Yoo[1]

[1]Department of Mechanical & Aerospace Engineering, Seoul National University, Seoul 151-744, Korea

[2]Institute of Advanced Machines and Design, Seoul National University, Korea

In some specific conditions, a flying spinning ball deflects in a direction opposite to that predicted by the Magnus effect, which is known as the inverse Magnus effect. To elucidate when and why this effect occurs, we measure the variations of the drag and lift forces on a rotating sphere and the corresponding flow field with the spin ratio (the ratio of the rotational velocity to the translational one). This counterintuitive phenomenon occurs because the boundary layer flow moving against the surface of a rotating sphere undergoes a transition to turbulence, whereas that moving with the rotating surface remains laminar. The turbulence energizes the flow and thus the main separation occurs farther downstream, inducing faster flow velocity there and generating negative lift force. Empirical formulae are derived to predict the location where the flow separates as a function of the Reynolds number and the spin ratio. Using the formulae derived, the condition for the onset of the inverse Magnus effect is suggested based on the negative lift generation mechanism.

Key words: separated flows, wakes/jets

1. Introduction

The Magnus effect is a well-known phenomenon by which a spinning ball moving through the air deflects in the direction of rotation (Magnus 1853). One can easily find the Magnus effect in many sports, such the baseball, golf, tennis, cricket and soccer (Mehta 1985). For example, in soccer, a ball spinning in the clockwise direction curves away from its principal flight path to the right. Applications of this effect are not limited to sports but include external ballistics (Swanson 1961), flying machines (Seifert 2012), ship stabilization (Morisseau 1985) and the saltation of particles (White & Schulz 1977). Moreover, the Magnus effect is exploited in a number of natural designs (Wauthy *et al.* 1998; Dickinson, Lehmann & Sane 1999; Vogel 2013).

† Email address for correspondence: choi@snu.ac.kr

J. Kim, H. Choi, H. Park and J. Y. Yoo

The inverse Magnus effect refers to the deflection of a flying spinning ball in the direction opposite to that predicted by the Magnus effect. This counterintuitive phenomenon occurs only at some specific Reynolds numbers ($Re = Ud/\nu$; U is the flying speed, d is the ball diameter and ν is the kinematic viscosity) and spin ratios ($\alpha = \omega d/2U$; ω is the spinning angular velocity). Many earlier studies (Maccoll 1928; Davies 1949; Taneda 1957; Briggs 1959; Tanaka, Yamagata & Tsuji 1990; Aoki *et al.* 2003*a*,*b*; Barlow & Domanski 2008; Kray, Franke & Frank 2012; Muto, Tsubokura & Oshima 2012*a*,*b*) have experimentally and numerically measured the inverse Magnus force, but no relationship between Re and α generating the inverse Magnus effect has been provided so far.

The classical explanation of the Magnus effect relies on the Bernoulli principle, which states that for an inviscid flow, an increase in the speed of the fluid occurs simultaneously with a decrease in the pressure and vice versa. However, since the concept of the boundary layer was introduced by Prandtl in 1904, the conventional Magnus effect has been explained in terms of a delayed separation on the retreating side where the sphere surface moves with the flow. Interestingly, when the inverse Magnus effect occurs, the flow separates farther downstream on the advancing side (the sphere surface moves against the flow) than on the retreating side (Taneda 1957; Kray *et al.* 2012; Muto *et al.* 2012*a*,*b*). This counterintuitive shift of the separation delay has been explained as being caused by the turbulence being generated only on the advancing side (Davies 1949; Krahn 1956; Taneda 1957; Briggs 1959; Aoki *et al.* 2003*a*,*b*; Barlow & Domanski 2008; Kray *et al.* 2012; Muto *et al.* 2012*a*,*b*), but the detailed process of the delayed separation has not been fully investigated due to the difficulty of quantitatively measuring the flow near the surface of a rotating sphere. To explain the asymmetric flow separation for the inverse Magnus effect, some authors (Davies 1949; Krahn 1956) have introduced the concept of the effective (or relative) Reynolds numbers on the advancing and retreating sides, i.e. $Re_{adv} = (U + \omega d/2)d/\nu = Re(1 + \alpha)$ and $Re_{ret} = (U - \omega d/2)d/\nu = Re(1 - \alpha)$, respectively. However, at a given Reynolds number, the return to a positive lift force after the inverse Magnus effect with increasing spin ratio could not be explained with these effective Reynolds numbers. Moreover, the conditions for the onset of the inverse Magnus effect, derived from the effective Reynolds numbers (Krahn 1956), did not match those from the experimental study (Swanson 1961).

In the present study, we investigate the mechanism of the inverse Magnus effect and suggest a predictive model for the onset of the effect by measuring the drag and lift forces directly from a rotating sphere by varying the Reynolds number and spin ratio, and the velocity fields near a rotating sphere surface using DPIV (digital particle image velocimetry).

2. Experimental set-up

Figure 1(*a*) shows the schematic diagram of the present experimental set-up for the force measurement. The experiment was conducted in a closed-type wind tunnel (Göttingen type), whose test section is 0.9 m wide, 0.9 m high and 4 m long. The maximum wind speed in the test section is 60 m s^{-1} and the uniformities of the mean streamwise velocity and the turbulence intensity are both within 0.3 % at a free-stream velocity of 18 m s^{-1}. The free-stream turbulence within 0.5 % is low and has little effect on the flow over a sphere in the Reynolds number range investigated in the present study (Son *et al.* 2010). The sphere with the diameter of 150 mm was made of acrylonitrile butadiene styrene (ABS) resin. A small DC motor was installed
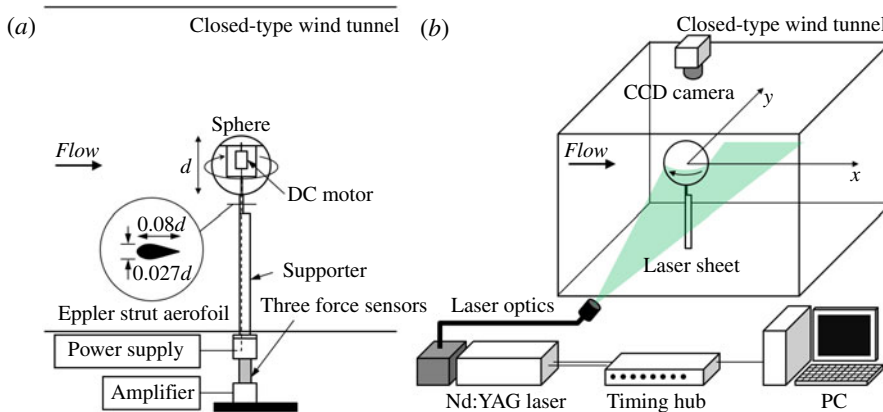
FIGURE 1. Schematic diagram of the experimental set-up for (*a*) the force measurement and (*b*) the DPIV measurement.

inside the sphere and rotated it about the vertical axis in the clockwise direction. The vibration of the sphere due to the rotation was minimized (less than 2 % of the sphere diameter) by preventing resonance in the system. The rotational speed of the sphere was varied by adjusting the voltage applied to the motor and was measured using a tachometer. The sphere with the motor was fixed to a supporter whose cross-section was designed as an Eppler strut aerofoil to minimize interference caused by the support. The drag and lift coefficients on a non-rotating sphere that are measured with the present experimental set-up are in good agreement with previous results (not shown here), ensuring negligible support interference on the forces measured.

The ranges of the Reynolds number and the spin ratio for the experiment were $Re = 0.6 \times 10^5$–1.8×10^5 and $\alpha = 0$ (no spin)–1.7, respectively. The three-dimensional forces on the sphere were measured simultaneously by three force sensors (one CAS BCL-3L and two AND LCB-03s) attached to the supporter. The calibration curve was linear and the uncertainty of the force measurement was $\pm 2.5\%$. The output from the force sensor was amplified and sampled for 60 s at a rate of 32 kHz to obtain the fully converged mean force. The data from the measurement were transferred to a computer through an A/D converter (NI PCI-6251), after which they were post-processed. The measured forces were corrected by subtracting those of the isolated supporter which were measured separately.

The velocity measurement was carried out in the same wind tunnel as was used for the force measurement. This facility was equipped with a glass wall and a transparent acrylic ceiling to provide the necessary optical access. As shown in figure 1(*b*), the DPIV system consisted of a fog generator (SAFEX), an Nd:YAG laser (New Wave) operating at 120 mJ, a CCD camera (Vieworks VH-4M) with a 2048 pixel × 2048 pixel resolution, and a timing hub (Integrated Design Tools). The fog generator produced liquid droplets of approximately 1 µm in diameter, which were introduced into the wind tunnel. A streamwise (*x*–*y*) centre plane parallel to the mean flow and normal to the axis of rotation was illuminated from one side of the test section with a thin laser light of 3 mm thickness using laser optics. The flow field in the shaded area behind the sphere was obtained by measuring the velocity fields while rotating the sphere in the counterclockwise direction. The camera used had a 60 mm lens to provide a 160 mm × 160 mm field-of-view (FOV). The camera

was mounted on a three-dimensional traversing unit which allowed it to be moved along the x and y directions. Eight FOVs were used to cover the velocity field of $-0.6 < x/d < 2.5$ and $-1 < y/d < 1$. An iterative cross-correlation analysis was conducted with an initial window size of 64 pixel $\times$ 64 pixel and with 32×32 final interrogation windows. The interrogation window was overlapped by 50 %, leading to a spatial resolution of $0.0086d$. Spurious vectors were removed using a local median filter that rejected vectors greater than three times the standard deviation of a 3×3 window. Removed vectors were replaced by vectors resulting from a linear interpolation in each direction from the surrounding 3×3 set of vectors.

3. Results and discussion

3.1. *Lift and drag variations*

The force coefficients on the rotating sphere are shown in figure 2. At a given Re, the lift coefficient, $C_L = L/(0.5\rho U^2 A)$, increases almost linearly with increasing spin ratio, where L is the lift, ρ is the density of air and A $(=\pi d^2/4)$ is the cross-sectional area of the sphere. However, with a further increase in α, the lift coefficient abruptly decreases at a critical spin ratio and then even becomes negative (i.e. the inverse Magnus effect). The critical spin ratio becomes smaller as the Reynolds number increases, and the magnitude of the negative lift force is greater for higher Reynolds number within the range of our experimental parameters. After it reaches its minimum, the lift coefficient increases and then becomes positive again. The spin ratio for the return to a positive lift force also decreases with increase in the Reynolds number. The behaviour of the drag coefficient, $C_D = D/(0.5\rho U^2 A)$, is quite similar to that of the lift coefficient in that it increases with the spin ratio, falls off and then increases again, where D is the drag. The drag coefficient starts to decrease at the same spin ratio as that at which the lift coefficient falls off, but it increases at a higher α than the lift coefficient. We will discuss this point in detail later in this paper.

3.2. *Mean and instantaneous velocity fields*

The variations of the forces on the sphere are directly associated with the separation points on both the retreating and the advancing surfaces. To observe the separation points, we measured the velocity field around the sphere by means of DPIV and estimated the separation angles (θ_{sep}) based on the MRS criterion (Rott 1956; Sears 1956; Moore 1958): $u_\theta = 0$ and $\partial u_\theta/\partial r = 0$, where (r, θ) are the polar coordinates with the origin at the centre of a sphere. As shown in figure 3(a) ($Re = 1.4 \times 10^5$), the separation angle on the retreating side (θ_{ret}) gradually increases with the spin ratio. On the other hand, on the advancing side, the separation angle (θ_{adv}) is smaller than that on the retreating side at low spin ratios, but rapidly increases to $\theta_{adv} = 140°$ at the critical spin ratio ($\alpha = 0.28$), much larger than θ_{ret} at the same spin ratio. At this critical spin ratio, the shear layer separated earlier on the advancing side reattaches to the rear surface of the sphere through turbulence generation from the shear-layer instability (figure 3c,i; see below). Main separation delay by this separation–reattachment process has also been found in other bluff-body flows and their controls (Jeon *et al.* 2004; Choi, Jeon & Choi 2006; Choi, Jeon & Kim 2008; Son *et al.* 2011). With this main separation delay, the radius of curvature, R, of the streamlines becomes smaller on the advancing side than that on the retreating side. The smaller R on the advancing side means a larger normal pressure gradient according to the so-called Euler-n equation, $\partial p/\partial n = \rho V^2/R$, where n is the local
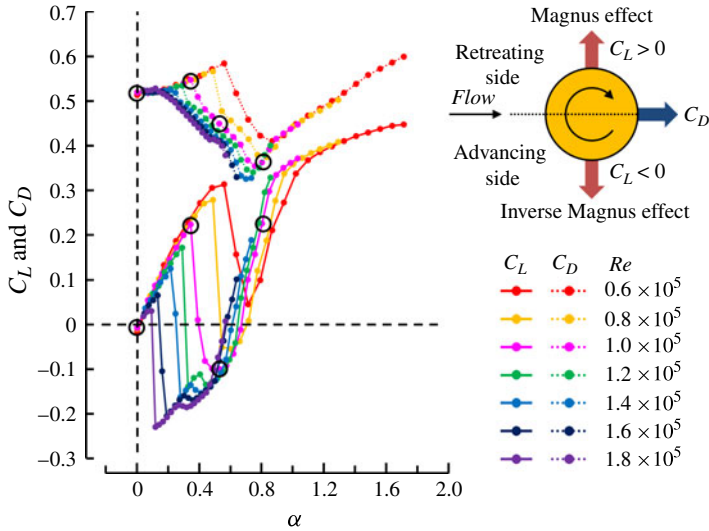
FIGURE 2. Variations of the lift and drag coefficients with the spin ratio at $Re = 0.6 \times 10^5$–1.8×10^5. The lift coefficient is defined to be positive when the lift force is exerted from the advancing to the retreating side (i.e. the Magnus effect occurs) and vice versa. It should be noted that the eight circles on the left of the figure denote the cases investigated in figure 4(*a–d*).

direction normal to the streamline and V is the local flow speed. Then, the pressure is smaller on the advancing side than on the retreating side, resulting in negative lift (figure 3*a*). With a further increase in the spin ratio, the separation angle on the retreating side continuously increases, whereas that on the advancing side decreases, resulting in an increase in C_L (figure 3*a*). To understand these separation-point movements according to the Reynolds number and the spin ratio, the instantaneous velocity vector fields near the separation point are measured and shown together with the normalized r.m.s. (root-mean-square) azimuthal velocity fluctuations in figure 3(*e–j*). On the retreating side (figure 3*e–g*), the sphere surface rotates in the same direction as the free stream and thus the momentum near the surface increases with the spin ratio. With the increased near-wall momentum, the separation point on the retreating side gradually moves downstream with the spin ratio (figure 3*a*). On the other hand, on the advancing side, at $\alpha = 0.21$ (figure 3*h*), the sphere surface rotates against the free stream and thus the flow loses its momentum near the surface, separating earlier than that on the retreating side. Therefore, the conventional Magnus effect with positive lift coefficient occurs at this spin ratio (figure 3*a*). However, at $\alpha = 0.28$ (figure 3*i*), the flow on the advancing side initially separates but reattaches due to the turbulence generation by the shear-layer instability. The reattached flow with high momentum near the wall overcomes the strong adverse pressure gradient formed on the rear sphere surface, resulting in a delay of the main separation. This flow phenomenon is critical in the sense that the drag and lift forces rapidly decrease. The formation of a secondary separation bubble, i.e. a closed-loop streamline consisting of separation and reattachment, is a typical phenomenon for the critical flow regime (Achenbach 1972; Choi *et al.* 2006, 2008; Son *et al.* 2011). With a further increase in the spin ratio, i.e. at $\alpha = 0.60$ (figure 3*j*), no secondary separation bubble is observed on the advancing side because a turbulent boundary-layer flow is formed without the formation of a separation bubble.
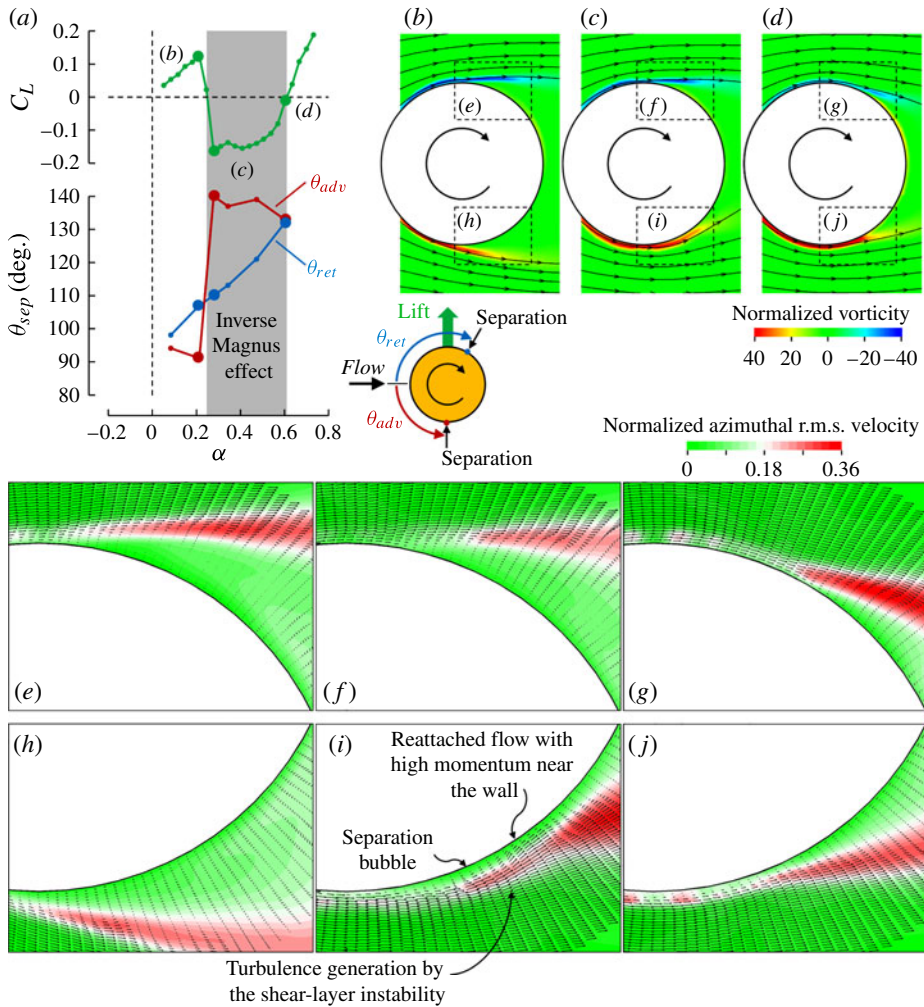
FIGURE 3. (a) Variations of the lift coefficient and separation angles on the retreating (θ_{ret}) and advancing (θ_{adv}) sides with the spin ratio at $Re = 1.4 \times 10^5$. Here, the separation angle is defined as the angle between the stagnation point and the separation point. (b–d) Time-averaged vorticity contours and streamlines at (b) $\alpha = 0.21$, (c) 0.28 and (d) 0.60. (e–j) Instantaneous velocity vectors and contours of the r.m.s. azimuthal velocity fluctuations on the retreating (e–g) and advancing (h–j) sides for (e,h) $\alpha = 0.21$, (f,i) 0.28 and (g,j) 0.60.

As mentioned previously, the drag coefficient starts to decrease at the same spin ratio as that at which the lift coefficient falls off, but starts to increase at a higher α than the lift coefficient (figure 2). To investigate why this occurs, we show the variation of the time-averaged streamlines with the spin ratio at $Re = 1.0 \times 10^5$ in figure 4(a–d). As the spin ratio increases from 0 (no spin) to 0.34, the separation delay occurs on the retreating side only, and the upper recirculation bubble inclines to the lower sphere surface with its centre closer to the surface (figure 4b), decreasing the pressure behind the sphere. Therefore, the drag coefficient increases at $\alpha = 0.34$ with a positive lift force (figure 2). At $\alpha = 0.53$, the separation on the advancing side is delayed more in the downstream than on the retreating side, and the
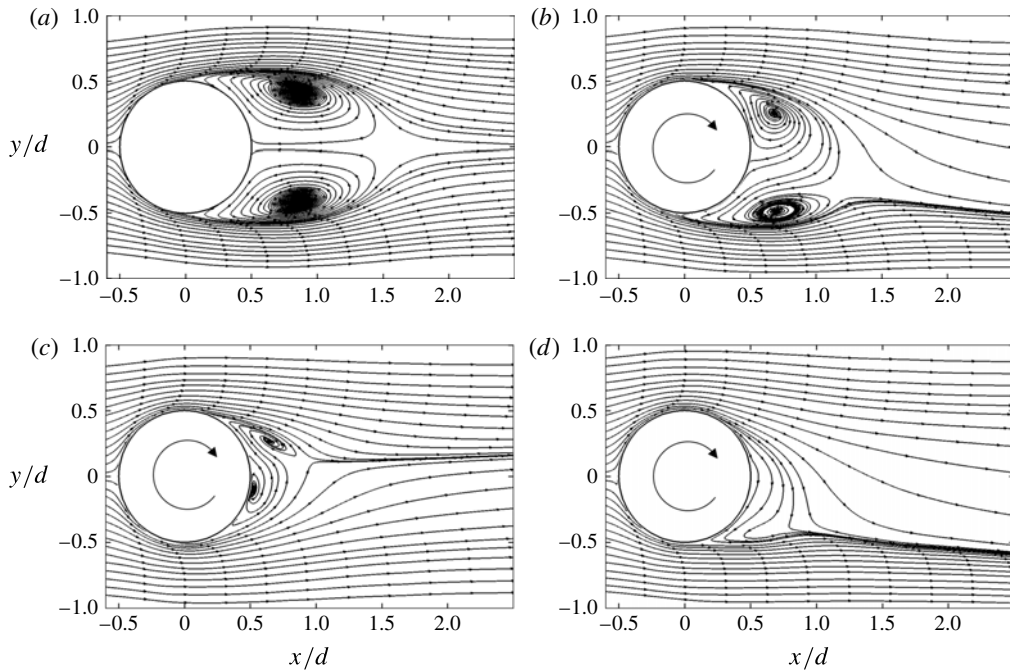
FIGURE 4. Time-averaged streamlines with the spin ratio at $Re = 1.0 \times 10^5$: (a) $\alpha = 0$ (no spin); (b) 0.34; (c) 0.53; (d) 0.80.

lower recirculation bubble moves closer to the surface (figure 4c). The shrinkage of recirculation bubbles is noticeable owing to the separation delay on both the retreating and the advancing sides, and thus the drag coefficient rapidly decreases with a negative lift force (figure 2). With a further increase in the spin ratio to $\alpha = 0.80$, the flow on the retreating side fully attaches to the surface, whereas the separation point on the advancing side moves upstream (figure 4d). Therefore, the lift coefficient becomes positive again and the drag coefficient decreases more (figure 2) in the absence of the recirculation bubble. At $\alpha > 0.80$, the separation point on the advancing side would move further upstream and thus both the drag and the lift coefficients would increase. It should be noted that the wake is deflected upwards with a negative lift force (figure 4c), whereas it is deflected downwards with a positive lift force (figure 4b,d).

3.3. *Predictive model of the inverse Magnus effect*

Given that the inverse Magnus effect occurs due to the change in the boundary-layer development on the advancing side, an important question is when this happens. To find the relationship between Re and α that generates the inverse Magnus effect, we derive an empirical relationship focusing on the variation of the separation angles on both sides of a rotating sphere. Figures 5(a,b) show the variations of the separation angles on the retreating and advancing sides with the spin ratio, respectively. On the retreating side, the separation angles at different Reynolds numbers collapse well into one line and increase with the spin ratio. This can therefore be expressed as a function of the spin ratio only, as follows:

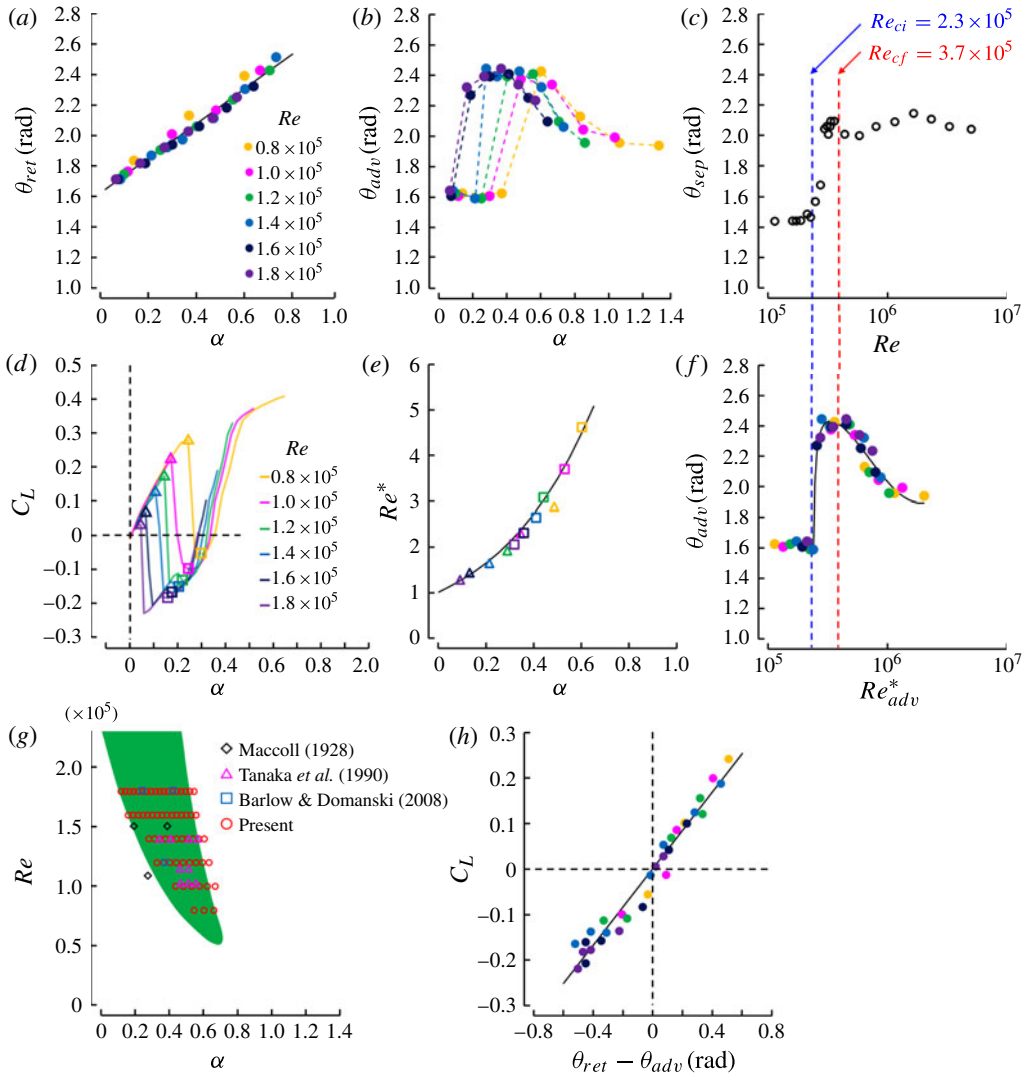$$\theta_{ret} = 1.14\alpha + 1.62 \ \text{(rad)}. \tag{3.1}$$

FIGURE 5. (*a*) Separation angle on the retreating side (θ_{ret}) with the spin ratio, $\theta_{ret} = 1.14\alpha + 1.62$ (solid line from best linear fit). (*b*) Separation angle on the advancing side (θ_{adv}) with the spin ratio. (*c*) Separation angle with the Reynolds number for a non-rotating sphere (Achenbach 1972). Here, Re_{ci} and Re_{cf} denote the initial and final Reynolds numbers for the critical flow regime, respectively. (*d*) Lift coefficient with the spin ratio. Here, the triangles and rectangles denote the initial and final spin ratios for the critical region on the advancing side. (*e*) Normalized effective Reynolds number ($Re^* = Re^*_{adv}/Re$) with the spin ratio, $Re^* = \exp(2.45\alpha)$ (solid line from best exponential fit). (*f*) Separation angle on the advancing side (θ_{adv}) with the effective Reynolds number, $\theta_{adv} = -0.016/\log(Re^*_{adv}/Re_{ci}) + 0.34\sin(2\pi \log(Re^*_{adv})/1.89 + 2.66) + 2.25$ (solid line from best fit). (*g*) Region of the inverse Magnus effect (green) on the Re–α plane derived from the condition $\theta_{adv} > \theta_{ret}$. Here, symbols denote the Re–α values where the measured lift coefficients were negative in the previous and present studies. (*h*) Lift coefficient as a function of the difference between the separation angles θ_{ret} and θ_{adv}, $C_L = 0.42(\theta_{ret} - \theta_{adv})$ (solid line from best linear fit).

This implies that the spin ratio is the most important parameter to determine the boundary-layer characteristics on the retreating side, irrespective of the Reynolds number. On the other hand, the separation angle on the advancing side is a function of both Re and α. The critical region for a non-rotating sphere is bounded by the initial and final critical Reynolds numbers, Re_{ci} and Re_{cf}, respectively, as shown in figure 5(c). The triangles in figure 5(d) denote the spin ratios at which sudden delay of separation occurs; that is, the effective Reynolds numbers at these α values equal Re_{ci}. The rectangles denote the spin ratios at which the separation bubble on the advancing side disappears; that is, the effective Reynolds numbers at these α's equal Re_{cf}. Thus, we newly model the effective Reynolds number on the advancing side as follows:

$$Re^*_{adv} = Re f(\alpha). \tag{3.2}$$

To find $f(\alpha)$, we plot the normalized effective Reynolds number $Re^* = Re^*_{adv}/Re$ with the spin ratio (figure 5e). This normalized effective Reynolds number can be fitted using the exponential function, $Re^* = Re^*_{adv}/Re = \exp(2.45\alpha)$. Consequently, the effective Reynolds number on the advancing side is expressed as a function of Re and α, as follows:

$$Re^*_{adv} = Re \exp(2.45\alpha). \tag{3.3}$$

Using the results obtained, we plot θ_{adv} versus Re^*_{adv} in figure 5(f). The separation angles from different Reynolds numbers collapse well into one curve (for $Re^*_{adv} > Re_{ci}$),

$$\theta_{adv} = -\frac{0.016}{\log(Re^*_{adv}/Re_{ci})} + 0.34 \sin\left(\frac{2\pi \log(Re^*_{adv})}{1.89} + 2.66\right) + 2.25 \ (\text{rad}), \tag{3.4}$$

and θ_{adv} rapidly increases when the effective Reynolds number is within the critical flow regime. The inverse Magnus effect occurs when the separation is delayed further more on the advancing side than on the retreating side. Therefore, we plot the region of the inverse Magnus effect on the Re–α plane from the modelled separation angles on the retreating and advancing sides using the following condition:

$$\theta_{adv} > \theta_{ret}. \tag{3.5}$$

Figure 5(g) shows the region of the inverse Magnus effect (green) on the Re–α plane, derived from (3.1), (3.4) and (3.5), together with the previous and present experimental results. As shown, the present model predicts the inverse Magnus effect very well. It should be noted that the modelled region is valid when the boundary-layer separation remains laminar on the retreating side (i.e. $Re < Re_{ci}$). Figure 5(h) shows the variation of the lift coefficient with the difference between the separation angles on the retreating and advancing sides. The lift coefficients at different Reynolds numbers and spin ratios collapse well into one line and increase linearly with $\theta_{ret} - \theta_{adv}$,

$$C_L = 0.42(\theta_{ret} - \theta_{adv}). \tag{3.6}$$

4. Summary and concluding remarks

In this paper, we have shown that the inverse Magnus effect is caused by the difference in the boundary-layer growth and separation along the advancing and retreating sphere surfaces. That is, at the critical spin ratio, the shear layer separated on the advancing side reattaches to the rear surface of the sphere through the transition to turbulence from the shear-layer instability, whereas the boundary-layer flow on the

retreating side remains laminar and separates earlier than that on the advancing side. By introducing an effective Reynolds number newly defined in the present study, we have provided the separation point as a function of the effective Reynolds number and suggested a predictive model of the inverse Magnus effect based on the negative lift generation mechanism.

Recently, lifting devices using the Magnus effect have received attention from the Society of Unmanned Aerial Vehicle (UAV) Design and Testing due to their high lift forces (or high wing loading) and stall resistance, despite the disadvantage of requiring additional driving mechanisms and complexity compared with conventional wings (Seifert 2012). The inverse Magnus effect occurs not only on a rotating sphere but also on rotating objects such as spheroids (Tanaka *et al.* 1990) and cylinders (Swanson 1961). A UAV designer thus should consider and avoid the inverse Magnus effect because small UAVs operate in the Reynolds number range of 10^4–10^5 based on the diameter of the cylinder-shaped rotor (Seifert 2012), at which breakdown of the lift force may occur. The present condition for the onset of the inverse Magnus effect should be helpful in the design of more effective and safer Magnus-force-based vehicles.

Acknowledgements

References

ACHENBACH, E. 1972 Experiments on the flow past spheres at very high Reynolds numbers. *J. Fluid Mech.* **54**, 565–575.

AOKI, K., KINOSHITA, Y., NAGASE, J. & NAKAYAMA, Y. 2003a Dependence of aerodynamic characteristics and flow pattern on surface structure of a baseball. *J. Vis.* **6**, 185–193.

AOKI, K., OHIKE, A., YAMAGUCHI, K. & NAKAYAMA, Y. 2003b Flying characteristics and flow pattern of a sphere with dimples. *J. Vis.* **6**, 67–76.

BARLOW, J. B. & DOMANSKI, M. J. 2008 Lift on stationary and rotating spheres under varying flow and surface conditions. *AIAA J.* **46**, 1932–1936.

BRIGGS, L. J. 1959 Effect of spin and speed on the lateral deflection (curve) of a baseball; and the Magnus effect for smooth spheres. *Am. J. Phys.* **27**, 589–596.

CHOI, J., JEON, W.-P. & CHOI, H. 2006 Mechanism of drag reduction by dimples on a sphere. *Phys. Fluids* **18**, 041702.

CHOI, H., JEON, W.-P. & KIM, J. 2008 Control of flow over a bluff body. *Annu. Rev. Fluid Mech.* **40**, 113–139.

DAVIES, J. M. 1949 The aerodynamics of golf balls. *J. Appl. Phys.* **20**, 821–828.

DICKINSON, M. H., LEHMANN, F.-O. & SANE, S. P. 1999 Wing rotation and the aerodynamic basis of insect flight. *Science* **284**, 1954–1960.

JEON, S., CHOI, J., JEON, W.-P., CHOI, H. & PARK, J. 2004 Active control of flow over a sphere for drag reduction at a subcritical Reynolds number. *J. Fluid Mech.* **517**, 113–129.

KRAHN, E. 1956 Negative Magnus force. *J. Aeronaut. Sci.* **23**, 377–378.

KRAY, T., FRANKE, J. & FRANK, W. 2012 Magnus effect on a rotating sphere at high Reynolds numbers. *J. Wind Engng Ind. Aerodyn.* **110**, 1–9.

MACCOLL, J. W. 1928 Aerodynamics of a spinning sphere. *J. R. Aero. Soc.* **28**, 777–798.

MAGNUS, G. 1853 Ueber die Abweichung der Geschosse, und: Ueber eine auffallende Erscheinung bei rotirenden Körpern. *Ann. Phys.* **164**, 1–29.

MEHTA, R. D. 1985 Aerodynamics of sports balls. *Annu. Rev. Fluid Mech.* **17**, 151–189.

MOORE, F. K. 1958 On the separation of the unsteady laminar boundary layer. In *Boundary Layer Research* (ed. H. G. Görtler), pp. 296–311. Springer.

MORISSEAU, K. C. 1985 Marine application of Magnus effect devices. *Nav. Engrs J.* **97**, 51–57.

MUTO, M., TSUBOKURA, M. & OSHIMA, N. 2012a Negative Magnus lift on a rotating sphere at around the critical Reynolds number. *Phys. Fluids* **24**, 014102.

MUTO, M., TSUBOKURA, M. & OSHIMA, N. 2012b Numerical visualization of boundary layer transition when negative Magnus effect occurs. *J. Vis.* **15**, 261–268.

ROTT, N. 1956 Unsteady viscous flow in the vicinity of a stagnation point. *Q. Appl. Maths* **13**, 444–451.

SEARS, W. R. 1956 Some recent developments in airfoil theory. *J. Aeronaut. Sci.* **23**, 490–499.

SEIFERT, J. 2012 A review of the Magnus effect in aeronautics. *Prog. Aerosp. Sci.* **55**, 17–45.

SON, K., CHOI, J., JEON, W.-P. & CHOI, H. 2010 Effect of free-stream turbulence on the flow over a sphere. *Phys. Fluids* **22**, 045101.

SON, K., CHOI, J., JEON, W.-P. & CHOI, H. 2011 Mechanism of drag reduction by a surface trip wire on a sphere. *J. Fluid Mech.* **672**, 411–427.

SWANSON, W. M. 1961 The Magnus effect: a summary of investigations to date. *Trans. ASME J. Basic Engng* **83**, 461–470.

TANAKA, T., YAMAGATA, K. & TSUJI, Y. 1990 Experiment of fluid forces on a rotating sphere and spheroid. In *Proceedings of the 2nd KSME–JSME Fluids Engineering Conference, Seoul, Korea, October*, pp. 10–13.

TANEDA, S. 1957 Negative Magnus effect. *Rep. Res. Inst. Appl. Mech.* **5**, 123–128.

VOGEL, S. 2013 *Comparative Biomechanics: Life's Physical World*. Princeton University Press.

WAUTHY, G., LEPONCE, M., BANAI, N., SYLIN, G. & LIONS, J.-C. 1998 The backward jump of a box moss mite. *Proc. R. Soc. Lond.* B **265**, 2235–2242.

WHITE, B. R. & SCHULZ, J. C. 1977 Magnus effect in saltation. *J. Fluid Mech.* **81**, 497–512.